frontiers in Chemistry

ORIGINAL RESEARCH
published: 16 August 2021
doi: 10.3389/fchem.2021.736369

A Facile Fabrication of $ZnFe_2O_4$/Sepiolite Composite with Excellent Photocatalytic Performance on the Removal of Tetracycline Hydrochloride

Caihong Zhang[1,2], *Xiaoyu Han*[1,2], *Fei Wang*[1,2], *Lijuan Wang*[1,2] *and Jinsheng Liang*[1,2]*

[1]Key Laboratory of Special Functional Materials for Ecological Environment and Information, Hebei University of Technology, Ministry of Education, Tianjin, China, [2]Institute of Power Source and Ecomaterials Science, Hebei University of Technology, Tianjin, China

The excellent photo-response of $ZnFe_2O_4$ in the visible light region makes it a promising catalyst, whereas some defects like serious particle agglomeration and easy recombination of photo-generated electron-hole pairs hinder its application. In this work, the $ZnFe_2O_4$/sepiolite (ZF-Sep) composites were synthesized using a co-precipitation method. The obtained ZF-Sep composites were characterized by XRD, SEM, TEM, FT-IR, XPS, BET, VSM and DRS. Moreover, the photocatalytic performance was evaluated by the tetracycline hydrochloride removal efficiency under simulated visible light illumination. The results displayed that the $ZnFe_2O_4$ with average sizes about 20 nm were highly dispersed on sepiolite nanofibers. All the composites exhibited better photocatalytic performance than pure $ZnFe_2O_4$ due to the synergistic effect of the improvement on the agglomeration phenomenon of $ZnFe_2O_4$ and the reduction on the recombination rate of photo-generated electrons and holes. The optimum removal efficiency was that of the ZF-Sep-11 composite, which reached 93.6% within 3 h. Besides, the composite exhibited an excellent stability and reusability. Therefore, ZF-Sep composite is a promising catalyst for the treatment of wastewater contained antibiotics.

Keywords: sepiolite nanofibers, $ZnFe_2O_4$, co-precipitation, photocatalytic, tetracycline hydrochloride

OPEN ACCESS

Edited by:
Bin Mu,
Lanzhou Institute of Chemical Physics (CAS), China

Reviewed by:
Yi Zhang,
Central South University, China
Shijie Li,
Zhejiang Ocean University, China
Wei Wei,
Jiangsu University, China

***Correspondence:**
Jinsheng Liang
liang_jinsheng@sina.com

Specialty section:
This article was submitted to Green and Sustainable Chemistry, a section of the journal Frontiers in Chemistry

Received: *05 July 2021*
Accepted: *02 August 2021*
Published: *16 August 2021*

Citation:
Zhang C, Han X, Wang F, Wang L and Liang J (2021) A Facile Fabrication of $ZnFe_2O_4$/Sepiolite Composite with Excellent Photocatalytic Performance on the Removal of Tetracycline Hydrochloride. Front. Chem. 9:736369. doi: 10.3389/fchem.2021.736369

INTRODUCTION

With the rapid expansion of pharmaceutical industry and breeding industry, the pollution of antibiotics and mycotoxins in the water environment has caused great concern. (Li et al., 2018; Das et al., 2020; Sun L. et al., 2020; Wang J. et al., 2020; Zhang et al., 2020). Because it is difficult to be metabolized by humans and animals, a large part of antibiotics are excreted in the form of urine and feces (Song et al., 2019). Hence, large quantities of antibiotics have been found in the soil, surface waters and even drinking water and will eventually threaten the health of humans and livestock through the food chain (Agerstrand et al., 2015; Isari et al., 2020a; Dong et al., 2020). Therefore, the removal of antibiotics from wastewater has been adopted, such as advanced oxidation processes (AOPs), membrane separation, microbial degradation, adsorption and photocatalysis (Debnath et al., 2020; Hayati et al., 2020; Khan et al., 2020; Wang Q. et al., 2020; Zhao R. et al., 2020; Zong et al.,

2021). Among above techniques, photocatalytic degradation of antibiotics on the surface of photocatalytic has been received a lot of attention because of their simple operation, high efficiency, energy saving, environmental protection and mild reaction conditions (Isari et al., 2020b). Semiconductor-based photocatalysis has attracted much attention due to their effective photocatalytic performance and environmental friendliness (Li et al., 2017; Li et al., 2020.). Traditional semiconductor materials, such as TiO_2, ZnO, ZrO_2, Fe_2O_3 and CdS are the most commonly used photocatalytic materials due to their strong oxidizing ability, stable chemical properties, and high photocatalytic activity (He et al., 2020; Jain et al., 2020; Reddy et al., 2020; Hunge et al., 2021). However, the low adsorption capacity, easy recombination of photo-generated electron-hole pairs, insufficient visible-light absorption and difficulty of recycling of these semiconductor materials hinders their practical application (Sun Z. et al., 2020; Xiao et al., 2020).

Zinc ferrite ($ZnFe_2O_4$), a typical spinel material, which possesses an AB_2O_4 structure with Zn^{2+} ions occupy tetrahedral A and Fe^{3+} ions occupy octahedral B site in a face-centered cubic unit cell (Lima et al., 2018). Zinc ferrite is a promising semiconductor photocatalytic material due to its excellent photo-response in the visible light region, considerable chemical stability and easy recycling performance (Casbeer et al., 2012; Tsay et al., 2019; Borade et al., 2020; Hu et al., 2020). Mishra et al. used the co-precipitation method to synthesize spinel zinc ferrite (SZFO) atomic sheets. With the aid of microwave irradiation, it showed excellent degradation performance for bright green, and the degradation efficiency was greater than 99% within 5 min (Mishra et al., 2019). Sun et al. used micro-nano bubbles and recyclable MFe_2O_4 (where M = Mn, Zn, Cu, Ni and Co) synthesized by a hydrothermal method to simultaneously remove SO_2 and NO_x from flue gas. The results show that MFe_2O_4 can accelerate the oxidation absorption of NO_x by producing OH. The NO_x removal efficiency increased from 32.85 to 83.88% in the NO_x-SO_2-MFe_2O_4-micro-nano bubble system, while the conversion rate of SO_2 can reach 100% at room temperature (Sun and Li, 2020). Mesoporous zinc ferrite, agglomeration of nanoparticles with size of 5–10 nm, was prepared by Su et al. In the presence of visible light and hydrogen peroxide, the degradation efficiency of AOII reaches almost 100% within 2 h (Su et al., 2012). However, insufficient photo degradation activity was exhibited to use $ZnFe_2O_4$ merely under visible light (Han et al., 2019; Nguyen et al., 2019; Wu and Zhang, 2019). Nowadays, lots of works, such as ion doping and forming the composites with other substances, have been reported to improve the photo catalytic performance (Ajithkumar et al., 2019; Peymani-Motlagh et al., 2019; Zhao Y. et al., 2020). Different kinds of substances were used to combine with $ZnFe_2O_4$ to form composites, which mainly included metal oxides (ZnO, TiO_2, Fe_2O_3, etc.) and carbon-based materials (reduced-graphene oxide, g-C_3N_4 and carbon nanotube, etc.). Moreover, the combination of $ZnFe_2O_4$ with more than one material has also attracted much attention. Enormous researches on the incorporation of $ZnFe_2O_4$ with mental oxides and carbon materials, silver species and carbon materials and inorganic-organic composite materials have been published recently. The introduction of these substances greatly improves the physical and chemical structure of $ZnFe_2O_4$, so that the optical, magnetic, catalytic and other properties were optimized (Adnan et al., 2021; Feng et al., 2021; Sun et al., 2017; Zia et al., 2020; Baynosa et al., 2020; Wang and Nan, 2019; Qin et al., 2017.). Compared with above mentioned substances, natural mineral materials have many advantages such as large specific surface area, abundant pore structure, strong adsorption capacity, large abundance and low cost, thereby they have great potential as catalyst carrier materials (Hu et al., 2019; Zhou et al., 2020).

Sepiolite, as a hydrous magnesium-rich silicate [$Si_{12}Mg_8O_{30}(OH)_4(OH2)_4{\cdot}8H_2O$], is a typical fibrous natural clay mineral with a layered chain structure. Sepiolite is composed of two silicon-oxygen tetrahedrons sandwiching a magnesium-oxygen octahedron and the discontinuity of the silicon-oxygen tetrahedron makes the sepiolite have a rich internal tunnel structure. Benefit from the unique structure and composition, sepiolite fibers possess large specific surface area, high porosity and various functional groups, which provides more reaction sites for supported catalysts (Ma and Zhang, 2016; Wang et al., 2017; Zhang et al., 2017; Mishra et al., 2019; Cui et al., 2020). In addition to its abundant storage, low cost and environmental friendliness, sepiolite is an ideal candidate for catalyst carrier (Xu et al., 2017). However, in order to increase surface area and enlarge its pore structure as well as to increase the number of active sites, an acid treatment is considered necessary before the synthesis process on raw sepiolite material. Therefore, the acid-treated sepiolite was often used to the support material for metal oxides TiO_2, ZnO, Fe_3O_4, Cu_2O, etc. (Xu et al., 2010; Zhu et al., 2012; Daneshkhah et al., 2017; Xu et al., 2019; Wang S. et al., 2020). In our pervious study, we have prepared $CoAl_2O_4$/sepiolite nanofibers composite and Co./$CoAl_2O_4$/sepiolite nanocomposite *via* different methods (Zhang et al., 2018; Wang F. et al., 2019; Hao et al., 2021; Wang et al., 2021). Nevertheless, as far as we know, there were few reports on sepiolite loaded $ZnFe_2O_4$ as a catalyst.

In this work, the $ZnFe_2O_4$ nanoparticles were grown on sepiolite nanofibers to obtain $ZnFe_2O_4$/sepiolite (ZF-Sep) composites by a co-precipitation method. Through different characterization of the composite and its photocatalytic performance for TCH, the influence of the structure of the composite on its performance was explored. This study provides a new idea for improving the performance of the catalysts and an inspiring approach for cost-effective preparation of highly efficient catalysts for wastewater containing antibiotics.

EXPREIMENTAL SECTION

Materials

Raw sepiolite was purchased from Henan province, and the main chemical compositions analyzed by XRF were 54.36% SiO_2, 35.6% MgO, 5.67% CaO and 1.36% Fe_2O_3. Hydrochloric acid (HCl), iron (III) nitrate nonahydrate [$Fe(NO_3)_3{\cdot}9H_2O$], zinc chloride ($ZnCl_2$), ammonia ($NH_3{\cdot}H_2O$), ethanol (CH_3CH_2OH), silver nitrate standard solution ($AgNO_3$,

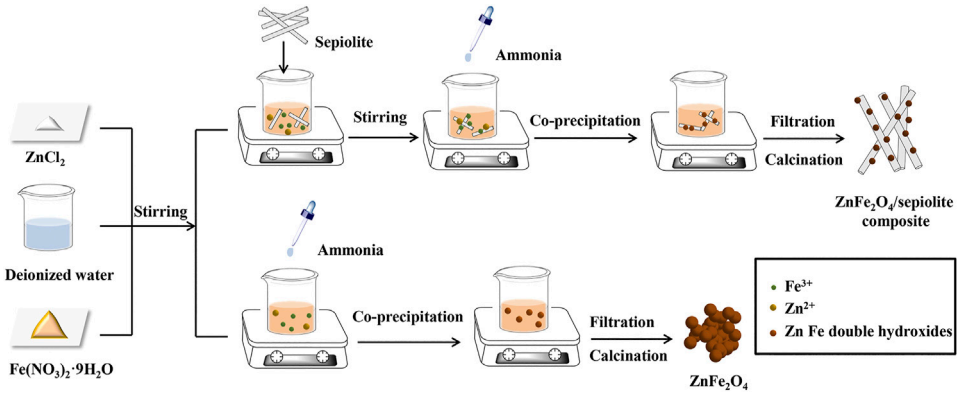

FIGURE 1 | Schematic for the fabrication of ZF-Sep composite.

0.1 mol/L), tetracycline hydrochloride (TCH), butyl alcohol (TBA), P-benzoquinone (BQ) and ammonium oxalate (AO) were analytical reagent and used without further purification.

Synthesis of $ZnFe_2O_4$ and ZF-Sep Composites

1.3629 g of $ZnCl_2$ and 8.08 g of $Fe(NO_3)_3 \cdot 9H_2O$ were dissolved in 100 ml deionized water, and a certain amount of sepiolite which were prepared by an acid treatment were added into the solution. Next, the pH of suspension was adjusted to 11 by adding aqueous ammonia dropwise. After aging for 12 h at room temperature, the precursor slurry was washed with ethanol and deionized water until the presence of chloride ions cannot be detected with silver nitrate standard solution. Then the filter cake was calcined in a muffle furnace for 3 h at 600°C. Finally, the $ZnFe_2O_4$/sepiolite composite (ZF-Sep) was obtained, and the schematic diagram was shown in **Figure 1**. On the other hand, pure $ZnFe_2O_4$ were also prepared by the same process. Samples were prepared with initial mass ratios of $ZnFe_2O_4$ to sepiolite nanofibers having values of 1:3, 1:2, 1:1, 2:1, 3:1, and labeled as ZF-Sep-13, ZF-Sep-12, ZF-Sep-11, ZF-Sep-21, ZF-Sep-31, respectively.

Characterization

Element analysis was carried out by ZSX Primusll X-ray fluorescence spectrometer (XRF). X-ray diffraction (XRD) patterns were employed to analyze the phase composition of samples by an X'Pert MPD dilatometer with CuKα radiation (40 Kv, 40 mA and $\lambda = 1.54180$ Å). The scanning was made in the 2θ range of 5–90° with a scanning speed of 12/min at room temperature. Scanning electron microscopy (SEM, JSM 7610F) and transmission electron microscopy (TEM, JEM-2010FEF, JEOL) were employed to observe the morphologies of the samples. Infrared radiation spectra of the as-prepared composites were obtained by a Fourier transform-infrared (FTIR) test spectrometer (Bruker VERTEX 80V) in the range of 4,000–400 cm^{-1} using KBr pellets. The X-ray photoelectron spectroscopy (XPS) measurements were performed on ESCALAB 250Xi (United States, Thermo Fisher Scientific) using a monochrome Al Kα (150 W, 20 eV pass energy, and 500 μm beam spot size). The magnetic property of the samples was measured by a vibrating sample magnetometer (VSM, Lakeshore VSM 7407) at room temperature. The surface area of the samples was tested by the physicochemical adsorption analyzer (United States, autosorb iQ). Diffuse reflectance ultraviolet-visible spectra (UV-vis DRS) were measured on a Shimadzu UV-1800 spectrophotometer.

Photocatalytic Performance

The photocatalytic performance of the as-prepared samples was evaluated by the removal efficiency of TCH under visible light irradiation. 0.1 g of catalyst was dispersed into 100 ml of TCH solution (20 mg/L). Before the suspension was subjected to irradiation by a 300 W Xe lamp ($\lambda > 420$ nm), stirring the produced suspension in the dark for half an hour to reach the adsorption/desorption equilibrium. Then, 3 ml of the suspension were extracted every 30 min and passed through a 0.22 micron filter membrane to remove the catalysts. The absorbance values at 357 nm of the filtrate were measured by a TU-1800 ultraviolet visible spectrophotometer. The removal efficiency can be calculated according to the following equation:

$$RE\% = \frac{(C_0 - C_t)}{C_0} \times 100\% \quad (1)$$

Where RE% represents the removal efficiency of catalyst, C_0 represents the TCH concentration at the beginning, and C_t represents the TCH concentration at a certain time t.

To detect the active species generated in the degradation process, the scavengers including butyl alcohol (TBA; 5 mmol/L), *p*-benzoquinone (BQ; 5 mmol/L), and ammonium oxalate (AO; 5 mmol/L) were added into the solution of TCH, respectively. The photocatalytic process was the same as that described above.

RESULTS AND DISCUSSION

Characterization of $ZnFe_2O_4$ and $ZnFe_2O_4$/Sepiolite Composites

The phase composition of samples was examined by XRD analysis. As shown in **Figure 2**, seven diffraction peaks (2θ) at

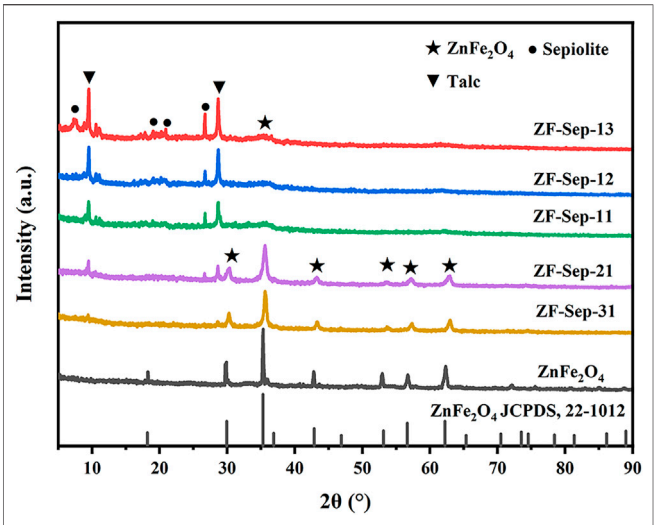

FIGURE 2 | XRD patterns of $ZnFe_2O_4$ and ZF-Sep composites with different $ZnFe_2O_4$ loadings.

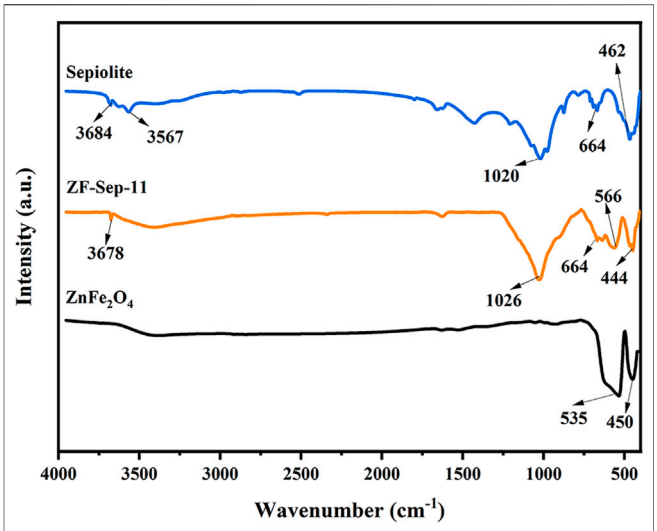

FIGURE 4 | FT-IR spectra of $ZnFe_2O_4$, Sepiolite and ZF-Sep-11.

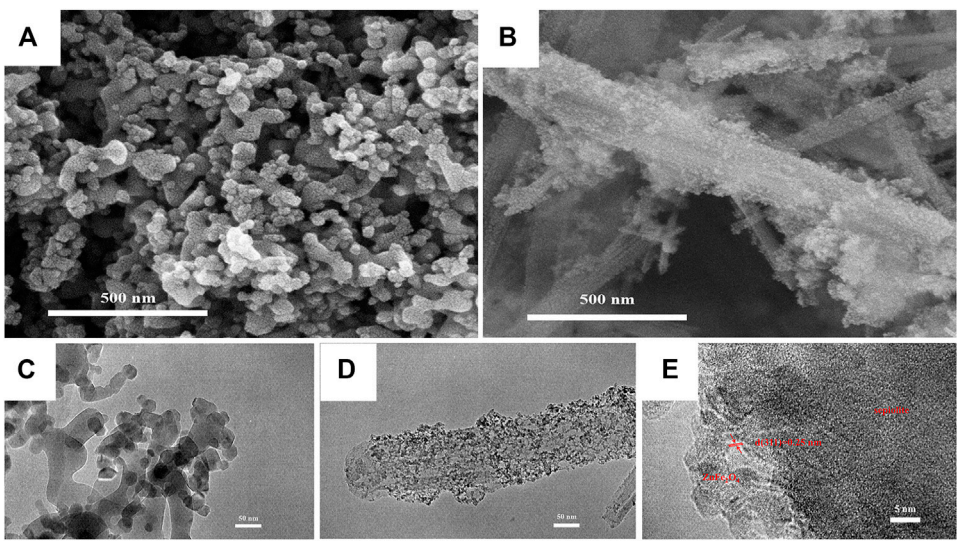

FIGURE 3 | SEM images of **(A)** $ZnFe_2O_4$ **(B)** ZF-Sep-11; TEM images of **(C)** $ZnFe_2O_4$ **(D)** ZF-Sep-11; HRTEM images of **(E)** ZF-Sep-11.

18.25°, 29.66°, 35.30°, 42.83°, 52.94°, 56.71° and 62.35° in curve of $ZnFe_2O_4$ correspond to the planes (111), (220), (311), (400), (422) (511) and (440) of $ZnFe_2O_4$, respectively. It confirms that single phase $ZnFe_2O_4$ (JCPDS No. 22-1012) with cubic spinel structure were synthesized successfully (Ma et al., 2019; Madhukara Naik et al., 2019). The characteristic peaks of sepiolite gradually decreased with the increase of the $ZnFe_2O_4$ content in the ZF-Sep composites, whereas the peaks intensity of $ZnFe_2O_4$ strengthened gradually, indicating that the co-existence of $ZnFe_2O_4$ and sepiolite in these composites. The decrease and broadening of diffraction peaks of $ZnFe_2O_4$ was derived from its dispersing in the surface of sepiolite. The decrease of sepiolite peak intensity was attributed to its imperfect crystalloid by disconnecting the fiber unit and the phase change of sepiolite to talc at the sintering temperature of 600°C (Xu et al., 2010).

The micromorphology of the $ZnFe_2O_4$ and ZF-Sep-11 composite were characterized by SEM and TEM. In **Figures 3A,C**, the images show that $ZnFe_2O_4$ sample was consisted of irregular nanoparticles with a size of about 20–200 nm. The existence of relatively large particles was attributed to the high specific surface energy of the nanoparticles causing serious agglomeration. As seen in **Figures 3B,D**, lots of small and irregular particles (about 20 nm) attached to the surface of sepiolite fibers, and the high resolution image (**Figure 3E**) displayed that the interface of $ZnFe_2O_4$ possessing obvious lattice fringes [d (311) = 0.25 nm] closely connected with the

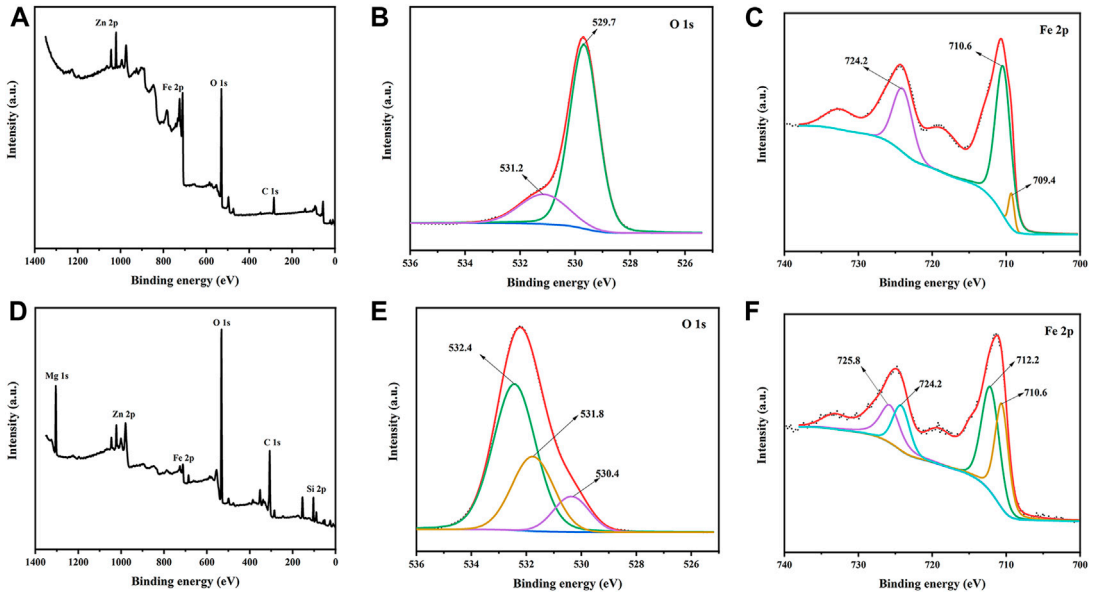

FIGURE 5 | XPS spectra of $ZnFe_2O_4$ **(A)** survey **(B)** O 1s spectrum **(C)** Fe 2p spectrum; and ZF-Sep-11 **(D)** survey **(E)** O 1s spectrum **(F)** Fe 2p spectrum.

interface of sepiolite which shows no obvious lattice fringes due to the low crystallinity. Consistent with the XRD results, SEM and TEM analysis also confirmed the successful synthesis of the composite, and the introduction of sepiolite fibers largely alleviated the agglomeration of $ZnFe_2O_4$. **Figure 4** shows the FTIR spectra of the sepiolite, $ZnFe_2O_4$ and ZF-Sep-11 composite. In the spectra of sepiolite, the bonds at 3,684–3,567 cm^{-1} and 664 cm^{-1} corresponded to the stretching and bending vibrations of Mg-OH in the Mg-O octahedral sheet. The bonds at 1,020 and 462 cm^{-1} were attributed to the stretching vibrations of Si-O bond in the Si-O-Si groups of the Si-O tetrahedral sheet (Zhang et al., 2014; Zhu et al., 2012.). There were two obvious peaks at 535 and 450 cm^{-1} in the spectra of $ZnFe_2O_4$, which could be ascribed to the stretching vibrations of the Zn-O bond and Fe-O bond in the spinel structure (Li J. et al., 2019; Mohan et al., 2020; Wang P. et al., 2019.). As shown in the spectra of ZF-Sep-11, the stretching vibrations of Si-O bond at 1,020 cm^{-1} shifted to 1,026 cm^{-1} and the stretching vibrations of Zn-O and Fe-O bands at 535 and 450 cm^{-1} shifted to 566 and 444 cm^{-1}, which was possible ascribed to the interaction between $ZnFe_2O_4$ and sepiolite nanofibers (Wang W. et al., 2019; Xu et al., 2017.).

The XPS method was employed to the $ZnFe_2O_4$ and ZF-Sep-11 composite sample to investigate its elemental composition and chemical states. As illustrated in **Figure 5A**, the survey spectrum of $ZnFe_2O_4$ shows the signal peaks of Fe 2p, Zn 2p, O 1s, indicating that Zn, Fe and O elements in the samples. Compared with $ZnFe_2O_4$, the appearance of Mg 1s and Si 2p indicated the introduction of sepiolite (**Figure 5D**). It is worth noting that the signal peaks of C 1s in the XPS survey spectrum are mainly caused by the external C impurities of XPS instrument. In **Figure 5B**, the O 1s spectrum of $ZnFe_2O_4$ could be divided into two peaks at approximately 529.7 and 531.2 eV, corresponding to the lattice oxygen and the oxygen absorbed on the surface, respectively (Wang S. et al., 2020). As shown in **Figure 5E**, the peak at 530.3 eV represented the lattice oxygen of $ZnFe_2O_4$, and that at 531.8 and 532.4 were attributed to the O atom of the -OH and Si-O-Si bond from sepiolite nanofibers. In the Fe 2p spectrum of $ZnFe_2O_4$ (**Figure 5C**), the peaks at 724.2 and 710.6 eV represented the Fe^{3+}, and 709.4 eV were attributable to the Fe^{2+} (Li Y. et al., 2019; Wang S. et al., 2020). Compared with $ZnFe_2O_4$, the peak positions of Fe^{3+} (725.8 and 712.2 eV) and Fe^{2+} (724.2 and 710.6 eV) had a certain shift, and the ratio of Fe^{3+} to Fe^{2+} was reduced (**Figure 5F**), which could be ascribed to the electron transfer and ion exchange between $ZnFe_2O_4$ and sepiolite nanofibers. Therefore, the sepiolite nanofibers in the composite might act as a good medium for the migration of photogenerated carriers in the reaction process, thereby reducing the recombination rate of photogenerated electrons and holes to increase the photocatalytic efficiency (Liu et al., 2015).

The nitrogen adsorption-desorption isotherms of sepiolite, $ZnFe_2O_4$ and ZF-Sep-11 composite were shown in **Figure 6A**, and the isotherms were in the shape of type IV, which indicated a typical of mesoporous materials. The result was further confirmed by the corresponding pore size distribution in **Figure 6B**. The specific surface area, total pore volume and average pore size of $ZnFe_2O_4$ and ZF-Sep composites with different loadings of $ZnFe_2O_4$ were summarized in **Table 1**. With the increase of the $ZnFe_2O_4$ loadings, the specific surface area of the composites showed a trend of first increasing and then decreasing, but all the composites were larger than pure $ZnFe_2O_4$. The optimal sample was ZF-Sep-11 composite, and its specific surface area was 138.3 m^2g^{-1}. The nitrogen adsorption-desorption isotherms also demonstrated that the introduction of sepiolite nanofibers improved the

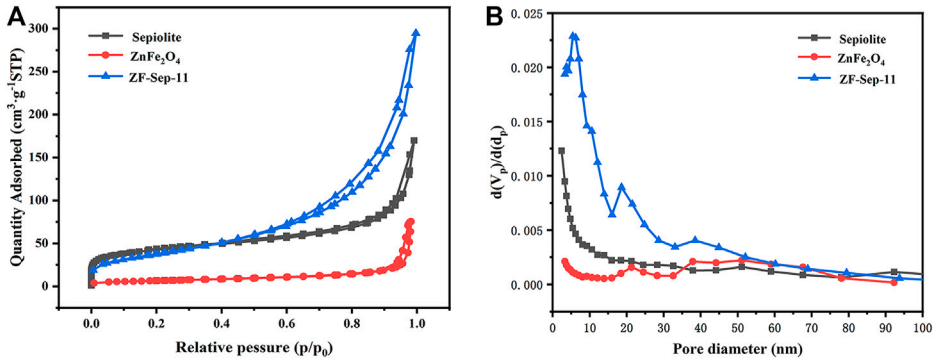

FIGURE 6 | (A) The N_2 adsorption-desorption isotherms, and **(B)** pore size distribution of sepiolite, $ZnFe_2O_4$ and ZF-Sep-11.

TABLE 1 | Textural parameters of $ZnFe_2O_4$, and the ZF-Sep composites with different contents of $ZnFe_2O_4$.

Sample	Specific surface area (m^2g^{-1})	Total pore volume (cm^3g^{-1})	Average pore diameter (nm)
$ZnFe_2O_4$	23.5	0.12	51.1
ZF-Sep-13	95.9	0.37	3.7
ZF-Sep-12	117.5	0.37	3.7
ZF-Sep-11	138.3	0.43	5.4
ZF-Sep-21	75.6	0.36	10.5
ZF-Sep-31	70.0	0.34	13.9

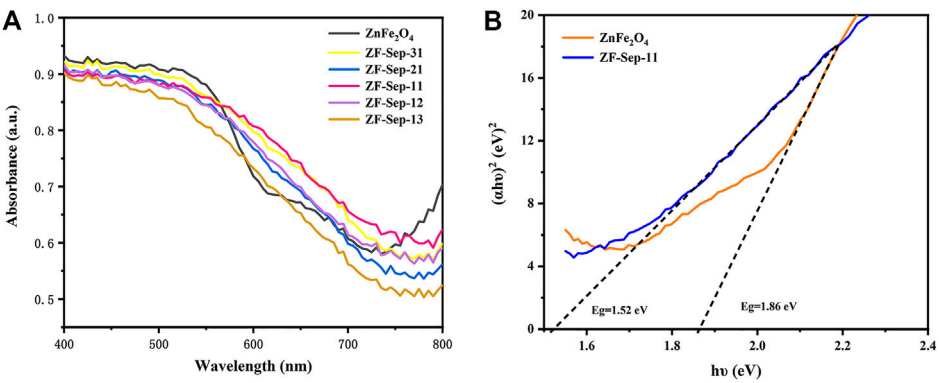

FIGURE 7 | (A) UV-vis spectra of $ZnFe_2O_4$ and ZF-Sep composites **(B)** Plots of $(\alpha h\nu)^2$ vs $h\nu$ of $ZnFe_2O_4$ and ZF-Sep-11.

agglomeration of $ZnFe_2O_4$, which increased the contact area with the target degradation product, thereby improved the photocatalytic performance.

The optical properties of the as-prepared samples were analyzed by UV-vis reflectance spectroscopy to evaluate the light absorption ability. As shown in **Figure 7A**, $ZnFe_2O_4$ and ZF-Sep composites presented significant absorbance in the 450–700 nm wavelength range. The band gap of ZF-Sep-11 composite could be estimated to be 1.52 eV, which was a little smaller than that of $ZnFe_2O_4$ (1.86 eV) (**Figure 7B**). In comparison with $ZnFe_2O_4$, ZF-Sep-11 composite showed the narrower band gap and higher light absorption, which could exhibit positive influence on the removal efficiency of target antibiotic in the visible light range.

The magnetic properties of the $ZnFe_2O_4$ and ZF-Sep-11 composite were measured by a vibrating sample magnetometer (VSM) with an applied magnetic field between −20,000 and 20,000 Oe at room temperature. **Figure 8** shows the plot of magnetization *versus* applied field with a small hysteresis loop which indicates that the samples display typical ferromagnetic (soft magnetic). The saturation magnetization (M_s) of $ZnFe_2O_4$ and ZF-Sep-11 composite were 51.693 and 34.780 emu/g,

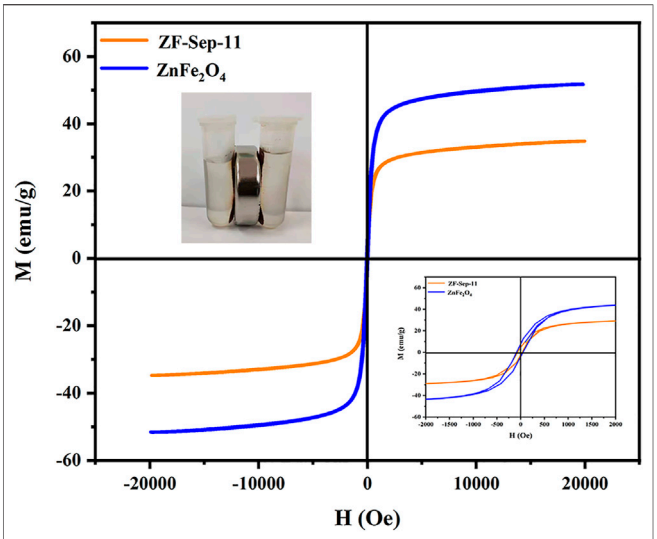

FIGURE 8 | Magnetization curves of $ZnFe_2O_4$ and ZF-Sep-11, inset show zoomed in version and the situation with an external magnetic field.

H_2O_2. The removal efficiency of tetracycline hydrochloride was 56.7% for $ZnFe_2O_4$ within 3 h. All of the composites exhibited superior removal efficiency for TCH compared with the single $ZnFe_2O_4$. Among these composites, ZF-Sep-11 showed the optical performance, and the removal efficiency of TCH reached 93.6% within 3 h. **Figure 9B** shows the reaction kinetics of the as-synthesized samples, in which the experimental data were in accordance with the pseudo first-order kinetic equation:

$$\ln(C_0/C) = kt \quad (3)$$

Where C_0 is initial concentration of TCH solution, C is the concentration of tetracycline hydrochloride at reaction time t, and t is the reaction time and k is the fitted kinetic rate constant. The values of kinetic rate constant of sepiolite, $ZnFe_2O_4$, ZF-Sep-31, ZF-Sep-21, ZF-Sep-11, ZF-Sep-12 and ZF-Sep-13 were 0.000248, 0.00293, 0.01057, 0.00686, 0.01504, 0.01188 and 0.00771 min^{-1}, respectively. ZF-Sep-11 showed the highest kinetic rate constant, which is about five times higher than that of signal $ZnFe_2O_4$.

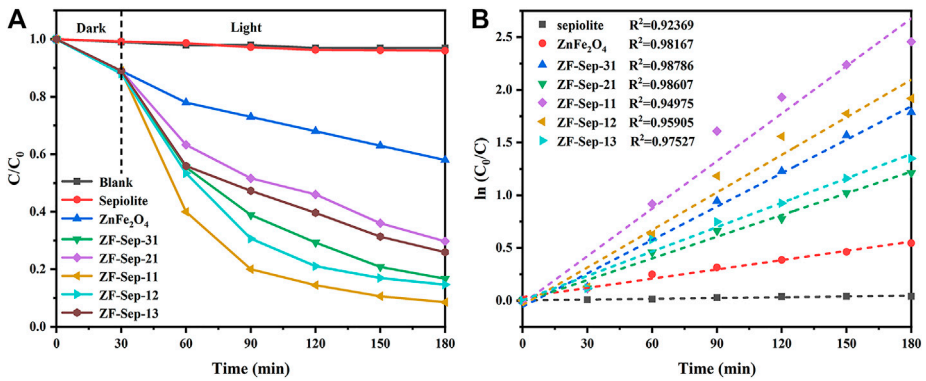

FIGURE 9 | (A) Removal of TCH under different systems, and **(B)** ln (C_0/C) *versus* reaction time for TCH under different conditions. Reaction conditions (TCH) = 20 mg/L (catalysts) = 1.0 g/L (H_2O_2) = 1 mM.

respectively. The decreasing of M_s mainly derives from the addition of non-magnetic material sepiolite. Due to the typical ferromagnetic, the catalyst could be efficiently removed from the aqueous solution of reaction mixture by an external magnet.

Photocatalytic Performance

The photocatalytic performance of the as-synthesized samples was evaluated by degrading TCH under visible light ($\lambda \geq$ 420 nm). The measured removal efficiency of the samples under different preparation conditions were depicted in **Figure 9**. As can be seen in **Figure 9A**, the removal efficiency of TCH solution was almost negligible when there was no catalyst and single sepiolite. For $ZnFe_2O_4$ and the composites, the decrease in the concentration of the TCH solution in the first 30 min in the absence of light may be due to the influence of the Fenton system formed by the addition of

Influence of Reaction Factors on Removal Efficiency of TCH

Different amounts of ZF-Sep-11 composite were used in the catalytic experiment to explore the effect of the catalyst content on the removal efficiency of TCH. The dosage of catalyst is set to 0.5, 1.0 and 1.5 g/L (the ratio of catalyst to TCH solution). In **Figure 10A**, when the dosage of catalyst was 0.5 and 1.5 g/L, the removal efficiency was 66.8 and 86.2% at 3 h, respectively, which were lower than the removal efficiency of 1.0 g/L (92.3%). The result means that too little catalyst dosage will cause the reduction of removal efficiency, because a small amount of active free radicals were generated. However, when an excessive amount of the catalyst was dispersed in the TCH solution, a small amount of light can reach their surface due to the influence of turbidity and scattering effect. The less exposed area under light may result in a decrease in overall catalytic efficiency.

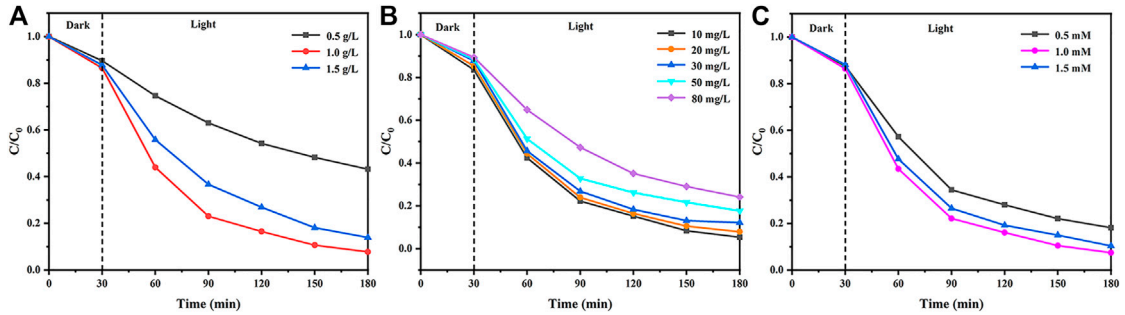

FIGURE 10 | Effect of **(A)** catalyst dosage **(B)** initial concentration, and **(C)** amount of H_2O_2 on the removal of TCH for ZF-Sep-11. Reaction conditions (TCH) = 20 mg/L (catalysts) = 1.0 g/L (H_2O_2) = 1 mM.

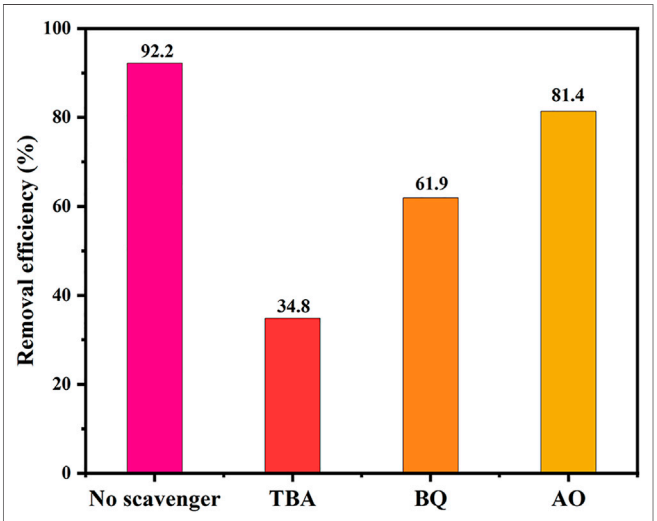

FIGURE 11 | Active species trapping experiment of ZF-Sep-11. Reaction conditions (TCH) = 20 mg/L [catalysts] = 1.0 g/L (H_2O_2) = 1 mM (TBA) = 5 mmM (BQ) = 5 mmM (AO) = 5 mmM.

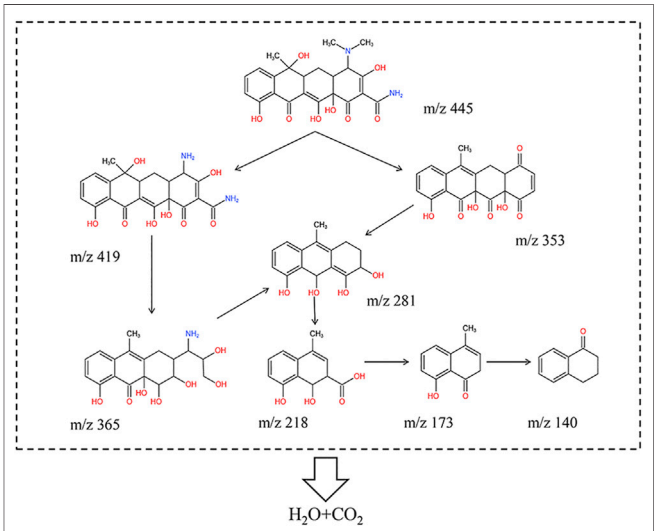

FIGURE 12 | Intermediates and reaction pathways of TCH photodegradation under visible light illumination over ZF-Sep-11.

Figure 10B showed the removal efficiency at different initial concentrations of TCH solution. The removal efficiency was 94.7, 92.2, 87.9, 82.4 and 75.9% in 3 h for 10, 20, 30, 50 and 80 mg/L of TCH solution, respectively. As the concentration increases, the removal efficiency of TCH gradually decreases. It could be attributed to the fact that the active sites on the surface of the catalyst are blocked in a high-concentration tetracycline solution.

In order to improve the ability to remove TCH, the amount of H_2O_2 added has been optimized. In **Figure 10C**, compared with the addition of 1 mM, when the addition of H_2O_2 was 0.5 and 1.5 mM, the removal efficiency were slightly reduced. Low H_2O_2 addition produces little free radicals. However, the excess H_2O_2 molecules will act as a quencher of OH to generate perhydroxyl (·OOH) radicals and compete with OOH to generate H_2O and O_2 (Su et al., 2012).

$$\cdot OH + H_2O_2 \rightarrow H_2O + \cdot OOH \quad (4)$$

$$\cdot OH + \cdot OOH \rightarrow H_2O + O_2 \quad (5)$$

Reactive Species of TCH Removal

In order to determine the main active species in the removal of TCH for ZF-Sep composite, free radical trapping experiments were implemented. BQ, IPA and AO were added as scavengers for O_2^-, ·OH and h^+, respectively. As depicted in **Figure 11**, the removal efficiency of TCH was 93.2% without any scavengers. After adding AO, there was no obviously decline in the removal efficiency of TCH (81.4%). However, the addition of TBA and BQ decreased the removal efficiency of TCH to 34.8 and 61.9%, respectively. The above results indicate that O_2^- and OH were the main active species in the removal process.

Possible Degradation Pathway

The liquid chromatography-mass spectroscopy (LC-MS) was used to analyze the possible intermediates that produced during the TCH degradation process to reveal the possible TCH degradation pathway. The LC-MS spectra displayed the

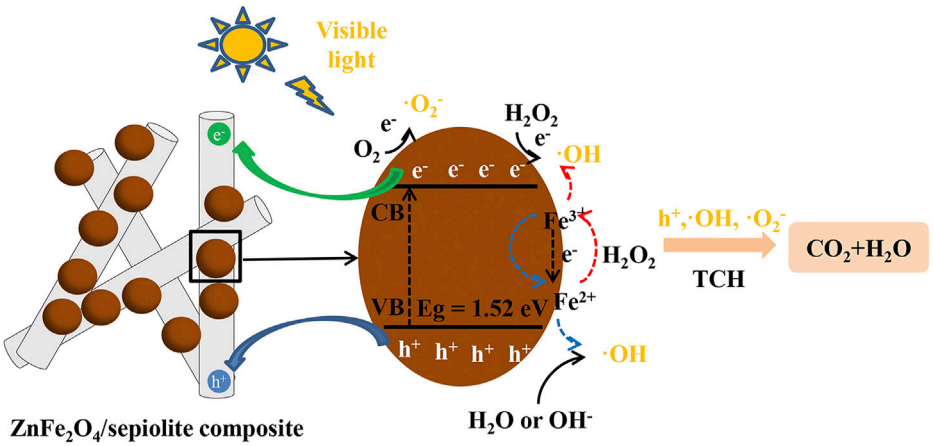

FIGURE 13 | Schematic diagram of possible mechanism.

formation of intermediate products with m/z values of 445, 419, 365, 353, 279, 218, 173, and 140 under visible light irradiation. According to the above results, the possible TCH degradation paths were proposed as shown in **Figure 12**. Firstly, TCH dissociates into tetracycline (TC) corresponding to m/z 445 in the aqueous solution (Lu et al., 2021). Due to the produced active species easily attack the amine group, hydroxyl group and methyl group in TC, the mass spectra corresponding to m/z 419 and m/z 353 were identified as the products formed from detachment of these groups of TC molecule. Secondly, the ring-opening products (m/z 365, m/z 281 and m/z 218) were assigned as the further oxidation products. Carboxyl group was detached from the ring-opening product (m/z 270) and then the intermediate product (m/z 140) was formed from the demethylation reaction (Pang et al., 2018; Li Z. et al., 2019.). Finally, these intermediate products were mineralized into CO_2 and H_2O *via* ring-opening reactions (Wu et al., 2021.).

Possible Mechanism

On the basis of the above analysis, a possible mechanism was shown in **Figure 13**. The loading of $ZnFe_2O_4$ on sepiolite nanofibers significantly improves its agglomeration phenomenon, which made more active sites in the surface of $ZnFe_2O_4$ were exposed, thereby improving its catalytic activity. Under visible light, the catalyst was activated to generate electron-hole pairs (**Eq. 6**). The sepiolite nanofibers might act as a good medium for the migration of photogenerated carriers to reduce the recombination rate of photogenerated electrons and holes. The holes were captured by OH^- or H_2O to generate OH, and O_2^- radicals were generated by trapping electrons for O_2 (**Eqs. 7–9**). In the presence of H_2O_2, it was more likely to trapping electrons to generate OH than O_2 (**Eq. 10**). Meanwhile, Fe^{3+} active sites were reduced by electrons to produce Fe^{2+} active sites which will activate H_2O_2 to produce regenerated Fe and new OH (**Eqs. 11–12**). Moreover, the generated Fe^{3+} reacted with OH^- to formed Fe^{2+} and OH (**Eq. 13**). Finally, TCH was degraded by the generated OH, $\cdot O_2^-$ and a small amount of h^+ (**Eq. 14**) (Li J. et al., 2019). Therefore, the synergistic effect of photochemical and catalytic reaction exists in the system of Vis-light/$ZnFe_2O_4$/sepiolite/H_2O_2.

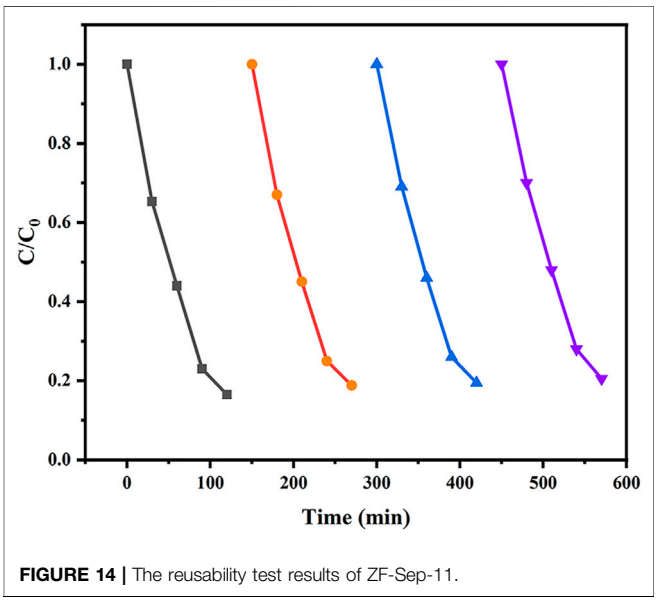

FIGURE 14 | The reusability test results of ZF-Sep-11.

$$\text{catalyst} + h_v \rightarrow \text{catalyst}\,(e^- + h^+) \quad (6)$$

$$h^+ + H_2O \rightarrow \cdot OH + H^+ \quad (7)$$

$$h^+ + OH^- \rightarrow \cdot OH \quad (8)$$

$$e^- + O_2 \rightarrow \cdot O_2^- \quad (9)$$

$$e^- + H_2O_2 \rightarrow \cdot OH + OH^- \quad (10)$$

$$e^- + Fe^{3+} \rightarrow Fe^{2+} \quad (11)$$

$$Fe^{2+} + H_2O_2 \rightarrow Fe^{3+} + \cdot OH + OH^- \quad (12)$$

$$Fe^{3+} + H_2O_2 \rightarrow Fe^{2+} + \cdot OOH + H^+ \quad (13)$$

$$h^+,\ \cdot OH,\ \cdot O_2^- + TCH \rightarrow CO_2 + H_2O \quad (14)$$

Stability of Catalyst

In order to explore the reusability and stability of the catalyst, four cycles of experiments were carried out. The degradation plots are shown in **Figure 14**, removal efficiency for the first cycle is 84.5%, second cycle is 81.2%, third cycle is 80.5%, and for the fourth cycle is 79.5%. It observed that there is no significant reduction in the removal efficiency. The above results show that the prepared catalyst has good recyclability and stability.

CONCLUSION

In summary, we have successfully prepared the ZF/Sep composites *via* a co-precipitation method. The introduction of sepiolite nanofibers significantly improved the agglomeration of $ZnFe_2O_4$ and reduced the recombination rate of photogenerated electrons and holes, so all the ZF-Sep composites presented better removal efficiency for TCH than pure $ZnFe_2O_4$. The most suitable removal efficiency of TCH (20 mg/L) appeared at 1.0 g/L ZF-Sep-11 catalyst dosage, and 1 mM H_2O_2 for 3 h. Besides, 79.5% of TCH removal efficiency could be still retained after four cycles, and the catalyst had soft magnetic properties and could be easily recovered when a magnetic field was applied. Thus, ZF/Sep composite display a promising photocatalysis performance in treating wastewater contained antibiotics.

DATA AVAILABILITY STATEMENT

The original contributions presented in the study are included in the article/supplementary material, further inquiries can be directed to the corresponding author.

AUTHOR CONTRIBUTIONS

CZ: Methodology, Validation, Formal analysis, Investigation, Data curation, Writing - original draft, Writing - review and editing. XH: Investigation, Data curation, Writing - review and editing, FW: Writing - review and editing. LW: Writing - review and editing. JL: Conceptualization, Writing - review and editing, Supervision, Project administration, Funding acquisition.

FUNDING

This work was supported by the Innovation Teams and Leading Talents Plan (Hebei, China).

REFERENCES

Adnan, M., Usman, M., Akram, M. A., Javed, S., Ali, S., Ahmad, I., et al. (2021). Study of Magnetic and Dielectric Properties of ZnFe2O4/CoCr2O4 Nanocomposites Produced Using Sol-Gel and Hydrothermal Processes. *J. Alloys Compd.* 865, 158953. doi:10.1016/j.jallcom.2021.158953

Ågerstrand, M., Berg, C., Björlenius, B., Breitholtz, M., Brunström, B., Fick, J., et al. (2015). Improving Environmental Risk Assessment of Human Pharmaceuticals. *Environ. Sci. Technol.* 49 (9), 5336–5345. doi:10.1021/acs.est.5b00302

Ajithkumar, P., Mohana, S., and Sumathi, S. (2019). Synthesis, Characterization, Optical and Photocatalytic Activity of Yttrium and Copper Co-doped Zinc Ferrite under Visible Light. *J. Mater. Sci. Mater. Electron.* 31 (2), 1168–1182. doi:10.1007/s10854-019-02628-8

Baynosa, M. L., Mady, A. H., Nguyen, V. Q., Kumar, D. R., Sayed, M. S., Tuma, D., et al. (2020). Eco-friendly Synthesis of Recyclable Mesoporous Zinc Ferrite@ reduced Graphene Oxide Nanocomposite for Efficient Photocatalytic Dye Degradation under Solar Radiation. *J. Colloid Interf. Sci.* 561, 459–469. doi:10.1016/j.jcis.2019.11.018

Borade, R. M., Somvanshi, S. B., Kale, S. B., Pawar, R. P., and Jadhav, K. M. (2020). Spinel Zinc Ferrite Nanoparticles: an Active Nanocatalyst for Microwave Irradiated Solvent Free Synthesis of Chalcones. *Mater. Res. Express* 7 (1), 016116. doi:10.1088/2053-1591/ab6c9c

Casbeer, E., Sharma, V. K., and Li, X.-Z. (2012). Synthesis and Photocatalytic Activity of Ferrites under Visible Light: A Review. *Sep. Purif. Technol.* 87, 1–14. doi:10.1016/j.seppur.2011.11.034

Cui, L., Hao, M., Wang, F., Fang, B., Liang, J., Zhu, M., et al. (2020). Microstructure Optimization of Mos2/Sepiolite Nanocomposites *via* a Surfactant-Assisted Hydrothermal Strategy for High Efficiency Photocatalysis. *Int. J. Photoenergy* 2020, 1–7. doi:10.1155/2020/8868782

Daneshkhah, M., Hossaini, H., and Malakootian, M. (2017). Removal of Metoprolol from Water by Sepiolite-Supported Nanoscale Zero-Valent Iron. *J. Environ. Chem. Eng.* 5 (4), 3490–3499. doi:10.1016/j.jece.2017.06.040

Das, K. K., Patnaik, S., Mansingh, S., Behera, A., Mohanty, A., Acharya, C., et al. (2020). Enhanced Photocatalytic Activities of Polypyrrole Sensitized Zinc Ferrite/graphitic Carbon Nitride N-N Heterojunction towards Ciprofloxacin Degradation, Hydrogen Evolution and Antibacterial Studies. *J. Colloid Interf. Sci.* 561, 551–567. doi:10.1016/j.jcis.2019.11.030

Debnath, B., Majumdar, M., Bhowmik, M., Bhowmik, K. L., Debnath, A., and Roy, D. N. (2020). The Effective Adsorption of Tetracycline onto Zirconia Nanoparticles Synthesized by Novel Microbial green Technology. *J. Environ. Manage.* 261, 110235. doi:10.1016/j.jenvman.2020.110235

Dong, S., Cui, L., Zhang, W., Xia, L., Zhou, S., Russell, C. K., et al. (2020). Double-shelled ZnSnO3 Hollow Cubes for Efficient Photocatalytic Degradation of Antibiotic Wastewater. *Chem. Eng. J.* 384, 123279. doi:10.1016/j.cej.2019.123279

Feng, J., Nian, P., Peng, L., Zhang, A., and Sun, Y. (2021). Degradation of Aqueous Methylparaben by Non-thermal Plasma Combined with ZnFe2O4-rGO Nanocomposites: Performance, Multi-Catalytic Mechanism, Influencing Factors and Degradation Pathways. *Chemosphere* 271, 129575. doi:10.1016/j.chemosphere.2021.129575

Han, J., Jun, B.-M., Heo, J., Kim, S., Yoon, Y., and Park, C. M. (2019). Heterogeneous Sonocatalytic Degradation of an Anionic Dye in Aqueous Solution Using a Magnetic Lanthanum Dioxide Carbonate-Doped Zinc Ferrite-Reduced Graphene Oxide Nanostructure. *Ecotoxicol. Environ. Saf.* 182, 109396. doi:10.1016/j.ecoenv.2019.109396

Hao, M., Gao, P., Liu, W., Fang, B., Liang, J., Zhang, T., et al. (2021). Microwave Hydrothermal-Reduction Synthesis of Zanthoxylum Trunk-like Co/CoAl2O4/sepiolite Nanocomposite. *Ceramics Int.* 47 (4), 4722–4728. doi:10.1016/j.ceramint.2020.10.041

Hayati, F., Isari, A. A., Anvaripour, B., Fattahi, M., and Kakavandi, B. (2020). Ultrasound-assisted Photocatalytic Degradation of Sulfadiazine Using MgO@CNT Heterojunction Composite: Effective Factors, Pathway and Biodegradability Studies. *Chem. Eng. J.* 381, 122636. doi:10.1016/j.cej.2019.122636

He, S., Yan, C., Chen, X.-Z., Wang, Z., Ouyang, T., Guo, M.-L., et al. (2020). Construction of Core-Shell Heterojunction Regulating α-Fe2O3 Layer on CeO2 Nanotube Arrays Enables Highly Efficient Z-Scheme Photoelectrocatalysis. *Appl. Catal. B: Environ.* 276, 119138. doi:10.1016/j.apcatb.2020.119138

Hu, X., Sun, Z., Song, J., Zhang, G., Li, C., and Zheng, S. (2019). Synthesis of Novel Ternary Heterogeneous BiOCl/TiO2/sepiolite Composite with Enhanced Visible-Light-Induced Photocatalytic Activity towards Tetracycline. *J. Colloid Interf. Sci.* 533, 238–250. doi:10.1016/j.jcis.2018.08.077

Hu, Z., He, Q., and Ge, M. (2020). Photocatalytic Degradation of Organic Contaminants by Magnetic Ag3PO4/MFe2O4 (M = Zn, Ni, Co) Composites: a Comparative Study and a New Insight into Mechanism. *J. Mater. Sci. Mater. Electron.* 32 (1), 827–842. doi:10.1007/s10854-020-04861-y

Hunge, Y. M., Yadav, A. A., Khan, S., Takagi, K., Suzuki, N., Teshima, K., et al. (2021). Photocatalytic Degradation of Bisphenol A Using Titanium Dioxide@nanodiamond Composites under UV Light Illumination. *J. Colloid Interf. Sci.* 582 (Pt B), 1058–1066. doi:10.1016/j.jcis.2020.08.102

Isari, A. A., Hayati, F., Kakavandi, B., Rostami, M., Motevassel, M., and Dehghanifard, E. (2020a). N, Cu Co-doped TiO2@functionalized SWCNT Photocatalyst Coupled with Ultrasound and Visible-Light: An Effective Sono-Photocatalysis Process for Pharmaceutical Wastewaters Treatment. *Chem. Eng. J.* 392, 123685. doi:10.1016/j.cej.2019.123685

Isari, A. A., Mehregan, M., Mehregan, S., Hayati, F., Rezaei Kalantary, R., and Kakavandi, B. (2020b). Sono-photocatalytic Degradation of Tetracycline and Pharmaceutical Wastewater Using WO3/CNT Heterojunction Nanocomposite under US and Visible Light Irradiations: A Novel Hybrid System. *J. Hazard. Mater.* 390, 122050. doi:10.1016/j.jhazmat.2020.122050

Jain, D., ShivaniBhojiya, A. A., Singh, H., Daima, H. K., Singh, M., et al. (2020). Microbial Fabrication of Zinc Oxide Nanoparticles and Evaluation of Their Antimicrobial and Photocatalytic Properties. *Front. Chem.* 8, 778. doi:10.3389/fchem.2020.00778

Khan, A. H., Khan, N. A., Ahmed, S., Dhingra, A., Singh, C. P., Khan, S. U., et al. (2020). Application of Advanced Oxidation Processes Followed by Different Treatment Technologies for Hospital Wastewater Treatment. *J. Clean. Prod.* 269, 122411. doi:10.1016/j.jclepro.2020.122411

Li, S., Shen, X., Liu, J., and Zhang, L. (2017). Synthesis of Ta3N5/Bi2MoO6core-Shell Fiber-Shaped Heterojunctions as Efficient and Easily Recyclable Photocatalysts. *Environ. Sci. Nano* 4 (5), 1155–1167. doi:10.1039/c6en00706f

Li, Y., Tian, G., Dong, G., Bai, S., Han, X., Liang, J., et al. (2018). Research Progress on the Raw and Modified Montmorillonites as Adsorbents for Mycotoxins: A Review. *Appl. Clay Sci.* 163, 299–311. doi:10.1016/j.clay.2018.07.032

Li, S., Xue, B., Chen, J., Jiang, W., and Liu, Y. (2020). BiOCOOH Microflowers Decorated with Ag/Ag2CrO4 Nanoparticles as Highly Efficient Photocatalyst for the Treatment of Toxic Wastewater. *Catalysts* 10 (1), 93. doi:10.3390/catal10010093

Li, J., Li, X., Zeng, L., Fan, S., Zhang, M., Sun, W., et al. (2019). Functionalized Nitrogen-Doped Carbon Dot-Modified Yolk-Shell ZnFe2O4 Nanospheres with Highly Efficient Light Harvesting and superior Catalytic Activity. *Nanoscale* 11 (9), 3877–3887. doi:10.1039/c8nr08611g

Li, Y., Chen, D., Fan, S., and Yang, T. (2019). Enhanced Visible Light Assisted Fenton-like Degradation of Dye *via* Metal-Doped Zinc Ferrite Nanosphere Prepared from Metal-Rich Industrial Wastewater. *J. Taiwan Inst. Chem. Eng.* 96, 185–192. doi:10.1016/j.jtice.2018.11.006

Li, Z., Guo, C., Lyu, J., Hu, Z., and Ge, M. (2019). Tetracycline Degradation by Persulfate Activated with Magnetic Cu/CuFe2O4 Composite: Efficiency, Stability, Mechanism and Degradation Pathway. *J. Hazard. Mater.* 373, 85–96. doi:10.1016/j.jhazmat.2019.03.075

Lima, E., Costa, L., Sampaio, G., Oliveira, E., Silva, E., Nascimento, H., et al. (2018). Zinc Ferrite Nanoparticles *via* Coprecipitation Modified Method: Glycerol as Structure Directing and Stabilizing Agent. *J. Braz. Chem. Soc.* doi:10.21577/0103-5053.20180225

Liu, T.-h., Chen, X.-j., Dai, Y.-z., Zhou, L.-l., Guo, J., Ai, S.-s., et al. (2015). Synthesis of Ag3PO4 Immobilized with Sepiolite and its Photocatalytic Performance for 2,4-dichlorophenol Degradation under Visible Light Irradiation. *J. Alloys Compd.* 649, 244–253. doi:10.1016/j.jallcom.2015.07.135

Lu, T., Gao, Y., Yang, Y., Ming, H., Huang, Z., Liu, G., et al. (2021). Efficient Degradation of Tetracycline Hydrochloride by Photocatalytic Ozonation over Bi2WO6. *Chemosphere* 283, 131256. doi:10.1016/j.chemosphere.2021.131256

Ma, Y., and Zhang, G. (2016). Sepiolite Nanofiber-Supported Platinum Nanoparticle Catalysts toward the Catalytic Oxidation of Formaldehyde at Ambient Temperature: Efficient and Stable Performance and Mechanism. *Chem. Eng. J.* 288, 70–78. doi:10.1016/j.cej.2015.11.077

Ma, J., Wang, X., Wang, G., and Wang, H. (2019). Zinc Ferrite Nanorod-Assembled Mesoporous Microspheres as Advanced Anode Materials for Sodium-Ion Batteries. *Energy Technol.* 7 (10), 1900479. doi:10.1002/ente.201900479

Madhukara Naik, M., Bhojya Naik, H. S., Nagaraju, G., Vinuth, M., Raja Naika, H., and Vinu, K. (2019). Green Synthesis of Zinc Ferrite Nanoparticles in Limonia Acidissima Juice: Characterization and Their Application as Photocatalytic and Antibacterial Activities. *Microchem. J.* 146, 1227–1235. doi:10.1016/j.microc.2019.02.059

Mishra, S., Sahu, T. K., Verma, P., Kumar, P., and Samanta, S. K. (2019). Microwave-Assisted Catalytic Degradation of Brilliant Green by Spinel Zinc Ferrite Sheets. *ACS Omega* 4 (6), 10411–10418. doi:10.1021/acsomega.9b00914

Mohan, H., Lim, J. M., Lee, S. W., Jang, J. S., Park, Y. J., Seralathan, K. K., et al. (2020). Enhanced Visible Light Photocatalysis with E-waste-based V 2 O 5/Zinc-Ferrite : BTEX Degradation and Mechanism. *J. Chem. Technol. Biotechnol.* 95 (11), 2842–2852. doi:10.1002/jctb.6442

Nguyen, T. B., Huang, C. P., and Doong, R.-a. (2019). Photocatalytic Degradation of Bisphenol A over a ZnFe2O4/TiO2 Nanocomposite under Visible Light. *Sci. Total Environ.* 646, 745–756. doi:10.1016/j.scitotenv.2018.07.352

Pang, Y., Kong, L., Lei, H., Chen, D., and Yuvaraja, G. (2018). Combined Microwave-Induced and Photocatalytic Oxidation Using Zinc Ferrite Catalyst for Efficient Degradation of Tetracycline Hydrochloride in Aqueous Solution. *J. Taiwan Inst. Chem. Eng.* 93, 397–404. doi:10.1016/j.jtice.2018.08.008

Peymani-Motlagh, S. M., Moeinian, N., Rostami, M., Fasihi-Ramandi, M., Sobhani-Nasab, A., Rahimi-Nasrabadi, M., et al. (2019). Effect of Gd3+-, Pr3+- or Sm3+-Substituted Cobalt-Zinc Ferrite on Photodegradation of Methyl orange and Cytotoxicity Tests. *J. Rare Earths* 37 (12), 1288–1295. doi:10.1016/j.jre.2019.04.010

Qin, M., Shuai, Q., Wu, G., Zheng, B., Wang, Z., and Wu, H. (2017). Zinc Ferrite Composite Material with Controllable Morphology and its Applications. *Mater. Sci. Eng. B* 224, 125–138. doi:10.1016/j.mseb.2017.07.016

Reddy, C. V., Reddy, I. N., Ravindranadh, K., Reddy, K. R., Shetti, N. P., Kim, D., et al. (2020). Copper-doped ZrO2 Nanoparticles as High-Performance Catalysts for Efficient Removal of Toxic Organic Pollutants and Stable Solar Water Oxidation. *J. Environ. Manage.* 260, 110088. doi:10.1016/j.jenvman.2020.110088

Song, Z., Ma, Y.-L., and Li, C.-E. (2019). The Residual Tetracycline in Pharmaceutical Wastewater Was Effectively Removed by Using MnO2/graphene Nanocomposite. *Sci. Total Environ.* 651 (Pt 1), 580–590. doi:10.1016/j.scitotenv.2018.09.240

Su, M., He, C., Sharma, V. K., Abou Asi, M., Xia, D., Li, X.-z., et al. (2012). Mesoporous Zinc Ferrite: Synthesis, Characterization, and Photocatalytic Activity with H2O2/visible Light. *J. Hazard. Mater.* 211-212, 95–103. doi:10.1016/j.jhazmat.2011.10.006

Sun, H., and Li, D. (2020). Recyclable MFe2O4 (M = Mn, Zn, Cu, Ni, Co) Coupled Micro-nano Bubbles for Simultaneous Catalytic Oxidation to Remove NOx and SO2 in Flue Gas. *RSC Adv.* 10 (42), 25155–25164. doi:10.1039/d0ra04392c

Sun, Y., Wu, X., Zhang, J., Zhao, Z., Li, H., Zhang, C., et al. (2017). Solvent-Mediated Preparation of Zinc Ferrite-Reduced Graphene Oxide Nanocomposites and its Application in Removal of Methylene Blue. *J. Nanosci Nanotechnol.* 17 (4), 2520–2524. doi:10.1166/jnn.2017.13894

Sun, L., Shao, Q., Zhang, Y., Jiang, H., Ge, S., Lou, S., et al. (2020). N Self-Doped ZnO Derived from Microwave Hydrothermal Synthesized Zeolitic Imidazolate Framework-8 toward Enhanced Photocatalytic Degradation of Methylene Blue. *J. Colloid Interf. Sci.* 565, 142–155. doi:10.1016/j.jcis.2019.12.107

Sun, Z., Huang, D., Duan, X., Hong, W., and Liang, J. (2020). Functionalized Nanoflower-like Hydroxyl Magnesium Silicate for Effective Adsorption of Aflatoxin B1. *J. Hazard. Mater.* 387, 121792. doi:10.1016/j.jhazmat.2019.121792

Tsay, C.-Y., Chiu, Y.-C., and Tseng, Y.-K. (2019). Investigation on Structural, Magnetic, and FMR Properties for Hydrothermally-Synthesized Magnesium-Zinc Ferrite Nanoparticles. *Physica B: Condens. Matter* 570, 29–34. doi:10.1016/j.physb.2019.05.037

Wang, X., and Nan, Z. (2019). Normal Spinel Structure ZnFe2O4/g-C3n4 Enhanced Catalytic Activity for Photo-Fenton Degradation of Methylene Blue. *Funct. Mater. Lett.* 12 (01), 1850108. doi:10.1142/s1793604718501084

Wang, F., Zhang, H., Liang, J., Tang, Q., Li, Y., and Shang, Z. (2017). High Emission Reduction Performance of a Novel Organic-Inorganic Composite Filters Containing Sepiolite mineral Nanofibers. *Sci. Rep.* 7, 43218. doi:10.1038/srep43218

Wang, F., Ding, Y., Hao, M., Fang, B., Liang, J., Zhang, T., et al. (2021). Novel Fabrication of a Sepiolite Supported Cobalt-Based Catalyst *via* a Coprecipitation-Reduction Method. *Appl. Clay Sci.* 200, 105909. doi:10.1016/j.clay.2020.105909

Wang, F., Gao, P., Liang, J., Zhang, T., Zhang, H., Ding, Y., et al. (2019). A Novel and Simple Microwave Hydrothermal Method for Preparation of CoAl2O4/sepiolite Nanofibers Composite. *Ceramics Int.* 45 (18), 24923–24926. doi:10.1016/j.ceramint.2019.08.191

Wang, J., Zhang, Q., Deng, F., Luo, X., and Dionysiou, D. D. (2020). Rapid Toxicity Elimination of Organic Pollutants by the Photocatalysis of Environment-Friendly and Magnetically Recoverable Step-Scheme SnFe2O4/ZnFe2O4 Nano-Heterojunctions. *Chem. Eng. J.* 379, 122264. doi:10.1016/j.cej.2019.122264

Wang, P., Qi, C., Hao, L., Wen, P., and Xu, X. (2019). Sepiolite/Cu2O/Cu Photocatalyst: Preparation and High Performance for Degradation of Organic Dye. *J. Mater. Sci. Technol.* 35 (3), 285–291. doi:10.1016/j.jmst.2018.03.023

Wang, Q., Cui, Y., Huang, R., Zhong, L., Yan, P., Zhang, S., et al. (2020). A Heterogeneous Fenton Reaction System of N-Doped TiO2 Anchored on Sepiolite Activates Peroxymonosulfate under Visible Light Irradiation. *Chem. Eng. J.* 383, 123142. doi:10.1016/j.cej.2019.123142

Wang, S., Ma, X., Liu, Y., Yi, X., Du, G., and Li, J. (2020). Fate of Antibiotics, Antibiotic-Resistant Bacteria, and Cell-free Antibiotic-Resistant Genes in Full-Scale Membrane Bioreactor Wastewater Treatment Plants. *Bioresour. Technol.* 302, 122825. doi:10.1016/j.biortech.2020.122825

Wang, W., Guo, S., Zhang, D., and Yang, Z. (2019). One-pot Hydrothermal Synthesis of Reduced Graphene Oxide/zinc Ferrite Nanohybrids and its Catalytic Activity on the thermal Decomposition of Ammonium Perchlorate. *J. Saudi Chem. Soc.* 23 (2), 133–140. doi:10.1016/j.jscs.2018.05.001

Wu, Q., and Zhang, Z. (2019). Visible-light-driven Mitigation of Antibiotic Oxytetracycline and Disinfection of *Escherichia coli* Using Magnetic Recyclable Ag-modified Zinc Ferrite/diatomite Ternary Hybrid Material. *J. Chem. Technol. Biotechnol.* 94 (8), 2537–2546. doi:10.1002/jctb.6048

Wu, S., Li, X., Tian, Y., Lin, Y., and Hu, Y. H. (2021). Excellent Photocatalytic Degradation of Tetracycline over Black Anatase-TiO2 under Visible Light. *Chem. Eng. J.* 406, 126747. doi:10.1016/j.cej.2020.126747

Xiao, R., Zhao, C., Zou, Z., Chen, Z., Tian, L., Xu, H., et al. (2020). *In Situ* fabrication of 1D CdS nanorod/2D Ti3C2 MXene Nanosheet Schottky Heterojunction toward Enhanced Photocatalytic Hydrogen Evolution. *Appl. Catal. B: Environ.* 268, 118382. doi:10.1016/j.apcatb.2019.118382

Xu, W. G., Liu, S. F., Lu, S. X., Kang, S. Y., Zhou, Y., and Zhang, H. F. (2010). Photocatalytic Degradation in Aqueous Solution Using Quantum-Sized ZnO Particles Supported on Sepiolite. *J. Colloid Interf. Sci.* 351 (1), 210–216. doi:10.1016/j.jcis.2010.07.052

Xu, Z., Jiang, H., Yu, Y., Xu, J., Liang, J., Zhou, L., et al. (2017). Activation and β-FeOOH Modification of Sepiolite in One-step Hydrothermal Reaction and its Simulated Solar Light Catalytic Reduction of Cr(VI). *Appl. Clay Sci.* 135, 547–553. doi:10.1016/j.clay.2016.10.035

Xu, X., Chen, W., Zong, S., Ren, X., and Liu, D. (2019). Atrazine Degradation Using Fe3O4-Sepiolite Catalyzed Persulfate: Reactivity, Mechanism and Stability. *J. Hazard. Mater.* 377, 62–69. doi:10.1016/j.jhazmat.2019.05.029

Zhang, G., Xiong, Q., Xu, W., and Guo, S. (2014). Synthesis of Bicrystalline TiO2 Supported Sepiolite Fibers and Their Photocatalytic Activity for Degradation of Gaseous Formaldehyde. *Appl. Clay Sci.* 102, 231–237. doi:10.1016/j.clay.2014.10.001

Zhang, Y., Wang, L., Wang, F., Liang, J., Ran, S., and Sun, J. (2017). Phase Transformation and Morphology Evolution of Sepiolite Fibers during thermal Treatment. *Appl. Clay Sci.* 143, 205–211. doi:10.1016/j.clay.2017.03.042

Zhang, T., Wang, F., Liang, J., Fang, B., Gao, P., Gao, G., et al. (2018). A Novel and Facile Impregnation-Combustion Fabrication of Spherical CoAl2O4 Supported on Sepiolite Nanofibers. *Ceramics Int.* 44 (16), 19543–19546. doi:10.1016/j.ceramint.2018.07.197

Zhang, S., Li, B., Wang, X., Zhao, G., Hu, B., Lu, Z., et al. (2020). Recent Developments of Two-Dimensional Graphene-Based Composites in Visible-Light Photocatalysis for Eliminating Persistent Organic Pollutants from Wastewater. *Chem. Eng. J.* 390, 124642. doi:10.1016/j.cej.2020.124642

Zhao, R., Ma, T., Zhao, S., Rong, H., Tian, Y., and Zhu, G. (2020). Uniform and Stable Immobilization of Metal-Organic Frameworks into Chitosan Matrix for Enhanced Tetracycline Removal from Water. *Chem. Eng. J.* 382, 122893. doi:10.1016/j.cej.2019.122893

Zhao, Y., An, H., Dong, G., Feng, J., Ren, Y., and Wei, T. (2020). Elevated Removal of Di-n-butyl Phthalate by Catalytic Ozonation over Magnetic Mn-Doped Ferrospinel ZnFe2O4 Materials: Efficiency and Mechanism. *Appl. Surf. Sci.* 505, 144476. doi:10.1016/j.apsusc.2019.144476

Zhou, F., Wang, H., Zhou, S., Liu, Y., and Yan, C. (2020). Fabrication of Europium-Nitrogen Co-doped TiO2/Sepiolite Nanocomposites and its Improved Photocatalytic Activity in Real Wastewater Treatment. *Appl. Clay Sci.* 197, 105791. doi:10.1016/j.clay.2020.105791

Zhu, Q., Zhang, Y., Lv, F., Chu, P. K., Ye, Z., and Zhou, F. (2012). Cuprous Oxide Created on Sepiolite: Preparation, Characterization, and Photocatalytic Activity in Treatment of Red Water from 2,4,6-trinitrotoluene Manufacturing. *J. Hazard. Mater.* 217-218, 11–18. doi:10.1016/j.jhazmat.2011.12.053

Zia, J., Riyazuddin, M., Aazam, E. S., and Riaz, U. (2020). Rapid Catalytic Degradation of Amoxicillin Drug Using ZnFe2O4/PCz Nanohybrids under Microwave Irradiation. *Mater. Sci. Eng. B* 261, 114713. doi:10.1016/j.mseb.2020.114713

Zong, Y., Ma, S., Xue, J., Gu, J., and Wang, M. (2021). Bifunctional NiAlFe LDH-Coated Membrane for Oil-In-Water Emulsion Separation and Photocatalytic Degradation of Antibiotic. *Sci. Total Environ.* 751, 141660. doi:10.1016/j.scitotenv.2020.141660

Conflict of Interest: The authors declare that the research was conducted in the absence of any commercial or financial relationships that could be construed as a potential conflict of interest.